Journal of
Materials Chemistry A

ROYAL SOCIETY
OF CHEMISTRY

PAPER

View Article Online
View Journal | View Issue

Cite this: *J. Mater. Chem. A*, 2023, **11**, 17112

Integrated multimodal microfluidic E-skin powered by synergistic tandem nanogenerators for sweat-based health monitoring and skin-temperature analysis†

Kai Han,‡ Dadong Zhang,‡ Wenbo Zhuang, Yanfen Wan * and Peng Yang *

Wearable sweat biosensors, as the only noninvasive and measurable body-fluid sensors, serve as a very important means to monitor an individual's health status and more dynamic molecular-level information. The pursuit of wearable sweat biosensors includes not only detecting sweat components, but also integrating multiple functions, such as sweat-based health monitoring, near-field transmission and being self-powered. In this paper, we firstly bring forth a new idea of integrating sweat monitoring and dual electrical generation (hydrovoltaic and moisture electricity generation) for a multifunctional flexible device as a sweat-based health monitoring electronic (E)-skin. Herein, besides sweat composition analysis, a hydrovoltaic electricity generator is employed to detect the amount of sweat for the first time, and a dual electricity generator is used for self-supply of energy and skin-surface temperature measurement. Synergistic tandem nanogenerators are constructed using biomass carbon materials, and the power generation voltage can reach about 500 mV and is relatively stable. Our sweat E-skin (SE-skin) has five main functional areas, realizing real-time monitoring of sweat volume, sweat composition analysis' skin-surface temperature measurement and power-supply functions. This new integrated design not only enables real-time monitoring of indicators of health in sweat, but also provides a new idea for future intelligent wearables for human beings.

Received 23rd March 2023
Accepted 14th May 2023

DOI: 10.1039/d3ta01755a

rsc.li/materials-a

1. Introduction

The pioneering revolution of healthcare management is moving toward personalized at-home monitoring and telemedicine in the times of the internet-of-things, which arose and boomed with flexible wearable electronics.[1–3] This noninvasive type of wearable device offers new approaches to obtaining useful physiological-indicator information privately and continuously in non-hospital scenarios, especially for early-stage disease diagnosis, postoperative real-time tracking, continuous monitoring of chronic diseases, and preventive treatment of diseases.[4–6] The current wearable biosensors are mainly placed into two categories:[7] (1) trackers of physiological signals, such as heartbeat,[8] blood pressure,[9] and temperature,[10] and (2) biochemical-parameter monitors, such as those for sustainable tracking of body metabolites in biological fluids like sweat,[11] tears,[12] and interstitial fluids.[13] It is noteworthy that sweat-sensor systems operating on the skin, so called sweat electronic (SE)-skins, as one of the noninvasive and measurable body-fluid sensors, have developed very rapidly and provide a continuous, real-time and nonintrusive means to monitor an individual's health status at the molecular level.[7,14–17]

Sweat is an important secretion of the body and contains a wealth of electrolytes, metabolites, trace elements, hormones and proteins, whose metabolite concentrations could serve as a measure of underlying sickness, disease progression, dehydration and mental stress.[18–22] A wearable SE-skin, which combines nanomaterials, nano-energy and flexible electronics, could solve problems associated with usage outside hospital without nursing staff; however, remaining challenges in sustainably detecting diverse signals are: (1) the requirement of a flexible substrate, such as microfluidic chips, which could allow convenient collection of sweat from the skin followed by processing and detection; (2) the requirement of an appropriate supply power to support continuous working and accurate monitoring; (3) the developing trend of multimodal operation of wearable devices, not only for continuous monitoring of glucose but also lactate, chloride, pH, skin temperature and even sweat flow rate.[23–25] So, researchers have been devoted to integrating suitable microfluidic substrates, renewable nanogenerator energy supplies, and diverse functions into one device

---

National Center for International Research on Photoelectric and Energy Materials, Yunnan Key Laboratory for Micro/Nano Materials & Technology, School of Materials and Energy, Yunnan University, Kunming 650091, China. E-mail: yfwan@ynu.edu.cn; pyang@ynu.edu.cn

† Electronic supplementary information (ESI) available. See DOI: https://doi.org/10.1039/d3ta01755a

‡ Both of the authors contributed equally to this work.

in order to develop multifunctional self-powered wearable monitors to realize their full capacity.[26,27]

For example, a type of wearable perspiration-analyzing device based on sweat flowing on ZnO nanoarrays was reported for actively monitoring physiological status without any batteries or other power supply, where the biological status transforms into output DC electrical signals as sensing information through a hydrovoltaic effect.[28] In addition, battery-free skin-interfaced microfluidic/electronic systems based on lactate and glucose biofuel cells were used for electrochemical, colorimetric and volumetric analysis of sweat; it could simultaneously power itself to drive a near-field communication (NFC) system, but this self-energy requires certain conditions and is not reusable.[29] Sweat directly contacts the electrodes, and the change in resistance is measured to monitor the amount of sweat, combining the electrical signal with the amount of sweat monitoring, but the sweat will continue to corrode the electrodes and reduce the service life.[30] There is another microfluidic system using a piezoelectric nanogenerator as a self-powered system, which was integrated into a flexible self-sustainable sweat sensor; the components in sweat are detected by ion-selective electrodes, and the two power generation modes are integrated, but the piezoelectric signal is unstable and susceptible to interference, resulting in unstable energy supply.[31] So, from the above-mentioned sweat sensors, there remain big challenges of sustainable self-supply of power, suitable substrates for touching skin and integration of multiple s.

The emerging pursuit of flexible SE-skins is to achieve multiple functions. According to the reported literature, some SE-skins already use multiple methods to detect the content of one or several components in sweat,[32,33] and some SE-skins can monitor the amount of sweat in real time.[34–37] However, there is a lot of health information related to sweat, and the analysis of one or several components and the amount of sweat alone cannot fully reflect sweat health. Therefore, there is a certain trend for the future development of this field to integrate several functions or even all functions on one piece of SE-skin.[38,39] However, the integrated functions are not simply merged. It is necessary to make a reasonable design according to the functions that need to be integrated, so that these functions can act at the same time without interfering with each other. At the same time, it is also necessary to make reasonable spatial arrangements for these functional areas, which are mainly dependent on the basic substrate design, such as programmable microfluidic chips.

Microfluidic chips are a special type of device used to process tiny amounts of fluids and can integrate various functions in one device, making them ideal for collecting sweat from skin and processing it.[40,41] At present, scientists have used microfluidic channels as the basic substrate to collect and measure sweat. For example, the use of capillary force to collect sweat into microfluidic channels and the use of colored reactions to detect chloride-ion content and pH in sweat enables real-time detection of indicators of health in human sweat (sweat health).[34] Other scientists have combined microfluidic channels with self-powered modules, such as biofuel cells and ion-selective electrodes, so that sweat can be used for self-powered energy while monitoring sweat health.[29,31] However, with the combination of the self-powering module and the microfluidic channel, it is not only necessary to ensure the normal operation of self-supply of energy, but also to improve the space utilization in the structural design.

For wearable electronic devices, power supply is one of the most important concerns.[42] Traditional wearable electronics use rigid batteries, which have the disadvantages of being inconvenient to wear and having poor deformability.[43] In contrast to conventional batteries, energy supply using renewable green energy sources can solve the above problems and provide a continuous power source, such as biofuel cells,[44–46] ion-selective batteries[29] and hydrovoltaic electricity generation,[28] which holds great potential for power supply in flexible wearable electronics. Among so many renewable green energy sources, benefitting from easy-utilization and sustainability, hydrovoltaic electricity generation and/or moisture electricity generation for energy supply are excellent candidates for flexible wearable electronic devices, especially for sweat monitoring.[47] The current hydrovoltaic electricity-generation devices can continuously generate a voltage of about 500 mV and have a fast response speed, so they can be used for the detection of the amount of fluid in a microfluidic channel and can be used for signal transmission.[48–50] The electricity generated by moisture electricity generation can last for a long time in the range of several hundred millivolts and can be used as a stable energy supply for electronic devices.[51–53] When water flows through a hydrovoltaic electricity-generation device to generate electricity, it will evaporate into the air. If it is combined with moisture electricity generation, the water can be recycled and the generated energy can be greatly increased.[54] In our work, we perform hydrovoltaic electricity generation and moisture electricity generation in sequence, realizing synergistic tandem nanogenerators, improving the water utilization rate and generating more electrical energy.

In this paper, for the first time, we propose an innovative design of a self-powered sweat E-skin based on a microfluidic channel that integrates multiple modules for sweat-volume monitoring, sweat-composition detection, temperature measurement and self-supply of energy (Fig. 1). Among these modules, colorimetric assay papers are used to measure the pH of the sweat as well as the chloride, glucose, lactate and uric-acid levels in a colorimetric module. The hydrovoltaic signal is employed to achieve sweat-flow statistics and self-supply of energy. Moisture electricity generation works for driving thermistors to measure skin-surface temperature. These functional modules work in a coordinated manner to facilitate sweat collection, sweat-based health monitoring, and self-power. The SE-skin we made is innovative in terms of functional integration and self-supplying methods, which has certain exploration significance for the development of wearable devices. It also has great potential to enable the collected sweat information to be directly transmitted to a mobile phone by self-supply of energy in the future.

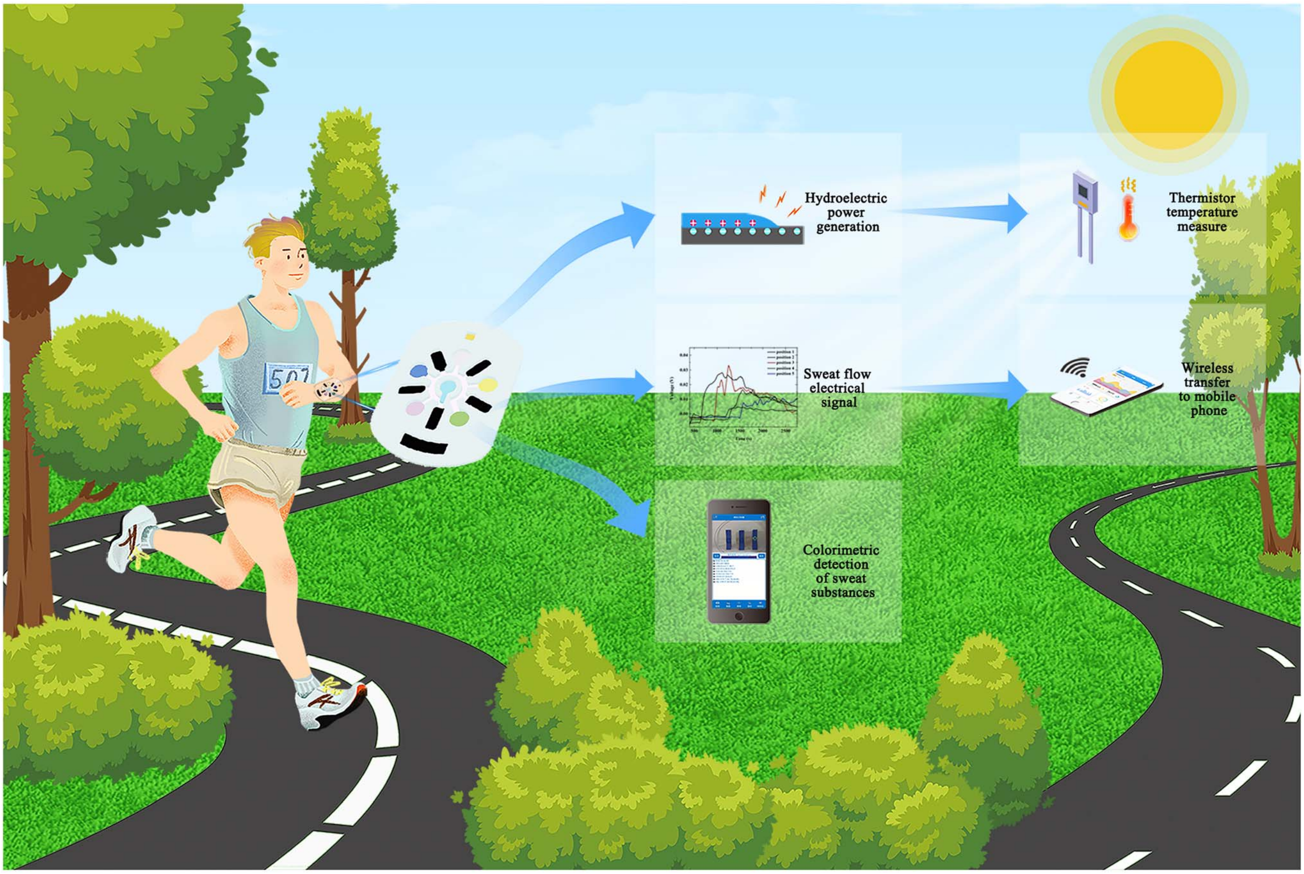

Fig. 1 Schematic diagram of sweat electronic skin (SE-skin) that has the functions of hydrovoltaic electricity generation to monitor sweat amount in real time, colorimetric assay papers to detect sweat composition, and moisture electricity generation to drive a thermistor.

2. Results and discussion

2.1 Structure and function of SE-skin

The flexible SE-skin consists of four main layer groups, as shown in Fig. 2(a). The first layer, from top to bottom, is a polydimethylsiloxane (PDMS) film, with a hole to absorb water vapor from the atmosphere for moisture electricity generation. The second layer is a microfluidic channel based in PDMS for absorbing and collecting sweat. This microfluidic channel also contains the hydrovoltaic electricity-generation module, moisture electricity generation supply, thermistor temperature-measurement module and colorimetric-assay-paper module; the main functions of this flexible electronic device are realized in this layer. The dual nanogenerators work on pomelo peel carbon (PPC) papers. The third layer is the electrode, which is connected to a signal acquisition device, collecting and analyzing the electrical signals generated from the hydrovoltaic electricity generator and thermistor, which is powered by moisture electricity generation. The fourth layer is an adhesive so that the SE-skin sits closely on the skin. At the same time, this layer has holes for the thermistor to form contact with the skin directly and to collect sweat from the skin.

As shown in Fig. 2(c), this SE-skin consists of five main functional areas: a microfluidic channel for collecting sweat, a hydrovoltaic electricity generation module and a moisture electricity generation module made of PPC paper, a temperature-measuring module made of a temperature-sensitive resistor, and a colorimetric-assay-paper module that can detect five types of sweat-component information (pH, chloride, glucose, lactate and uric acid). The thickness of the flexible electronic device is about 2 mm, the diameter of the sweat inlet is 6 mm, the internal aperture diameter is 2 mm, the chamber for the PPC paper is 4.5 mm × 10 mm and the diameter of the chamber for the colorimetric assay papers is 7 mm. We have also provided chambers at both ends of the channel for the thermistor and PPC paper where the moisture electricity generation module based on PPC paper connects to the microfluidic channel *via* a pressure valve.[55] The valve switches on once an external force is exerted, which allows the sweat to flow into the moisture electricity generation area and activate the moisture electricity generation module. Under the action of the ions in the sweat, the PPC paper absorbs water vapor from the surroundings through the holes reserved for it, which allows the moisture electricity generation module to produce a steady output to supply the thermistor to detect the skin-surface temperature.

The operation process of our SE-skin is shown in Fig. 2(d). Firstly, the SE-skin is attached to human skin, and as the person

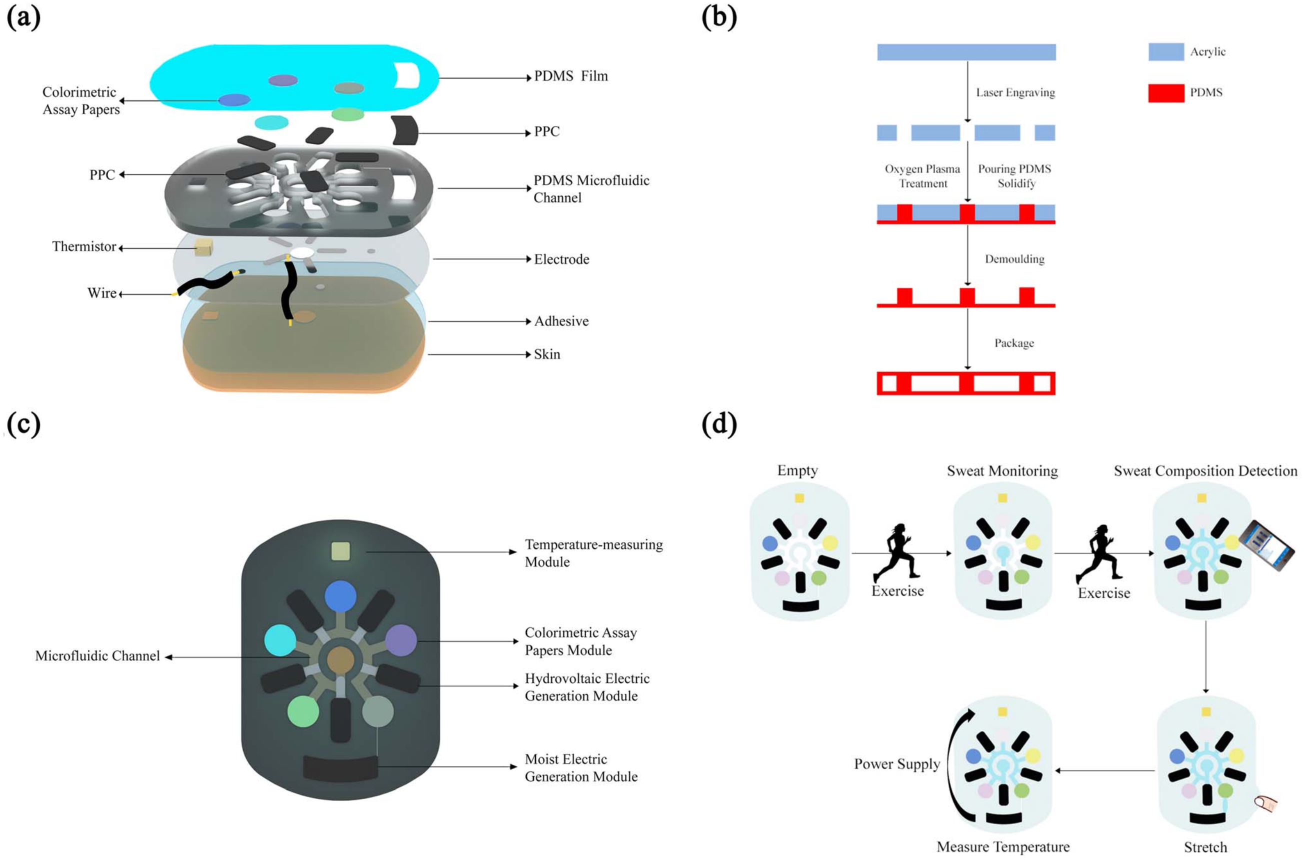

Fig. 2 Schematic images of the structure and function of the SE-skin in this work. (a) Layered structure of the SE-skin. (b) Fabrication of the microfluidic channel. (c) Functional areas of the flexible SE-skin. (d) Operation mode of the flexible SE-skin.

sweats during exercise, sweat enters the SE-skin through the central sweat absorption part. In this process, the amount of sweat is increasing, and the sweat in the SE-skin gradually fills each area. According to the electrical signal collected from the hydrovoltaic electricity generation module, the amount of sweat in this part of the human skin can be indirectly indicated. At the same time, according to the result of the colored reaction of the colorimetric assay papers, the content of each substance in the sweat and its pH value are determined by color-recognition software on a mobile phone. When sweat fills the entire internal chamber of the SE-skin, the pressure valve is switched on, stretching the patch and allowing a small amount of sweat to enter the area used for moisture electricity generation, which activates the moisture electricity generation module and provides the thermistor with power; the temperature of the human skin in this area is monitored by analyzing the electrical signals collected from the thermistor.

2.2 Properties of the PPC papers

In order to make the performance of the PPC papers outstanding and stable, we have carried out a lot of research. There are many factors that affect the final effect of the hydrovoltaic generator, with the size of the pores and the number of surface functional groups being the crucial elements, where a smaller pore size and more surface groups will make the hydrovoltaic effect stronger.[56–59] In order to make the pores reach a suitable size, we have improved the preparation method. Fig. S1† illustrates the preparation process of the PPC papers. The pomelo peel was carbonized under the protection of nitrogen, then the obtained toner was ball-milled and treated with chloroacetic acid. Finally, the treated toner was evenly smeared on paper and treated with ink and PSSA (poly(styrene sulfonic acid)). The produced PPC paper's morphology is shown in Fig. S2(a)† is the PPC paper without ball milling, and Fig. S2(b) and (c)† are the PPC paper after ball milling. It can be seen that the specific surface area of the PPC paper increases and the pore size decreases after ball milling, which increasingly benefits the hydrovoltaic effect.

Surface treatments such as acid leaching and oxygen plasma bombardment were applied to the PPC paper to make a large number of oxygen-containing groups appear on the surface, which is beneficial to improving the hydrovoltaic electricity generation. Surface-group characterization methods such as FTIR (Fourier transform infrared spectroscopy) and XPS (X-ray photoelectron spectroscopy) show that the chloroacetic-acid-treated pomelo-peel carbon surfaces have not only hydroxyl groups but also carboxyl groups (Fig. S3 and S4†). Based on previous research, Raman I_D/I_G ratios (where I_D and I_G are the D-band and G-band Raman intensities) are widely used to evaluate the quality of carbon materials.[5] The ratio of the I_D and I_G peaks of the chloroacetic-acid-treated PPC paper is about 0.98, while the ratio of the I_D and I_G peaks of the sulfuric-acid-treated PPC paper is about 0.96 (the specific data is shown in Table S1†). So, we can reach the conclusion that the graphitization of the chloroacetic-acid-treated PPC paper is higher than that of the sulfuric-acid-treated PPC paper. The coexistence of amorphous and graphitized carbon facilitates the enhancement of electrical conductivity, thus improving the hydrovoltaic effects of the devices. Zeta potential tests also indicated that the chloroacetic-acid-treated PPC paper's surface had more negative surface charges (Fig. S5†).

We tested the hydrovoltaic performance of the PPC paper before and after soaking with ink (Fig. S6†). The test results show that the hydrovoltaic voltage of the PPC paper soaked with ink is about 50 mV higher than that without soaking in ink. Combined with the surface topography shown in Fig. S2(d)–(f),† we infer that the nanoscale carbon particles in the ink fill the pores of the PPC material after soaking in the ink, making the pore size smaller and thereby improving the hydrovoltaic performance. We also tested the effect of the substrate, biomass carbon content, and size of PPC papers on hydrovoltaic performance, as shown in Fig. S7.† The results show that, compared with cotton, paper gives better hydrovoltaic performance as the substrate of PPC papers. When the biomass carbon content is 0.03 g per 4 cm × 4 cm paper, its hydrovoltaic electricity generation voltage reaches its peak value. When the paper size is 2 cm × 4 cm, the hydrovoltaic electricity generation voltage is the highest and very stable.

In addition to the structure and surface characteristics of the device itself, the supply of water is also the basis for the hydrovoltaic effect of the device. In order to investigate in depth the interaction between the PPC paper and a stable water body, the output voltage of the hydrovoltaic device with a continuous water supply was tested. The test system is shown in Fig. S8(b),† where a section of PPC papers is inserted into a water sample while the two ends are connected to the source meter through copper-sheet electrodes. By comparing the hydrovoltaic electricity generation performance of PPC papers with different surface modifications, it was concluded that the highest voltage was generated by the chloroacetic-acid-treated pomelo-peel carbon (Fig. S8(a)†), which generated an open-circuit voltage of 150 mV within 2.5 days (Fig. S8(b)†). To investigate the interaction between the PPC paper and a small amount of water, the output voltage of a hydrovoltaic device with drops of simulated sweat and deionized water was tested. The hydrovoltaic voltage generated by deionized water droplets is unsustainable compared to the hydrovoltaic voltage generated by a continuous water supply. Over 3000 s, as the water droplets evaporate, the driving force of the hydrovoltaic effect gradually decreases and the output voltage gradually drops to 0. For the PPC paper treated with chloroacetic acid, the open-circuit voltage generated by simulated sweat was more persistent than that of deionized water, indicating that the ions in sweat have an influence on the hydrovoltaic effect. Then, we explored the interaction between the PPC-paper device and sweat.

The principle of hydrovoltaic electricity generation is shown in Fig. 3(a) illustrates the hydrovoltaic effect of sweat on the PPC paper. When sweat flows through it, the positive ions in the sweat and the carboxyl groups on the surface of the PPC material attract each other, and the negative ions and the carboxyl groups repel each other, forming an electric double layer (EDL), thereby generating a potential difference. As shown in Fig. 3(b), on the same PPC paper, the hydrovoltaic electricity generation of sweat and deionized water is different, due to the ion concentration in sweat being much larger than that of deionized water. According to the jump mechanism, the diffusion rate of hydrogen ions and hydroxide ions in solution is much higher than that of other ions. Due to the high degree of graphitization and negative surface charges on the surface of PPC treated with chloroacetic acid, more hydrated hydrogen ions can be generated in DI water. This may result in a phenomenon where the hydrovoltaic electricity generation by DI water is higher than the generation by simulated sweat at the beginning of water contact with the PPC treated with chloroacetic acid. After a period of time, the hydrovoltaic electricity generation by DI water gradually decreases as the water evaporates.

Interestingly, for the PPC paper, ions not only have a direct effect on its hydrovoltaic voltage, but also the accumulation of ions may have other influences on the performance of the device. Through adding simulated seawater to the PPC paper several times at hourly intervals (Fig. S9(a)†), continuous and regular voltage variation was tested, where the voltage gradually increased with the accumulation of ions on the device as the simulated seawater was added. This is mainly due to the increase in the ion concentration, which increases the zeta potential, and so increases the electric field generated by the electric double layer and the potential gradient formed.[56] In particular, when the fourth drop of simulated seawater was added, the voltage of the device dropped to 0.23 V and then remained constant for 8 hours, where it exhibited a much longer duration than the hydrovoltaic voltage generated by deionized water droplets. Afterwards, with the addition of the fifth drop of simulated seawater, the voltage rose again to 0.38 V (Fig. 3(c)). The reason why the voltage remains constant after a certain amount of decrease is that there exists a mechanism to maintain this potential difference besides the hydrovoltaic effect. From previous reports,[60–63] it was found that this additional mechanism is moisture electricity generation. The specific process is that with the fourth drop of simulated seawater added, a large number of ions have accumulated on the PPC paper, and because these ions are inherently hygroscopic, water molecules from the air are captured into the device, providing a constant supply of water to the device (Fig. 3(d)). The principle of moisture electricity generation is shown in Schematic 1 in the ESI.† At the same time, due to the gradient of water content at both ends of the device, the water flow gradually diffuses toward the end with lower water content, so that drives the movement of hydrated hydrogen ions in the water and establishes a potential difference.

Fig. 3(e) illustrates the dynamic open-circuit voltages generated by adding 50 μL of simulated sweat droplets with different pH values to seven PPC-paper devices under room temperature and ambient moisture conditions (25 °C, RH =

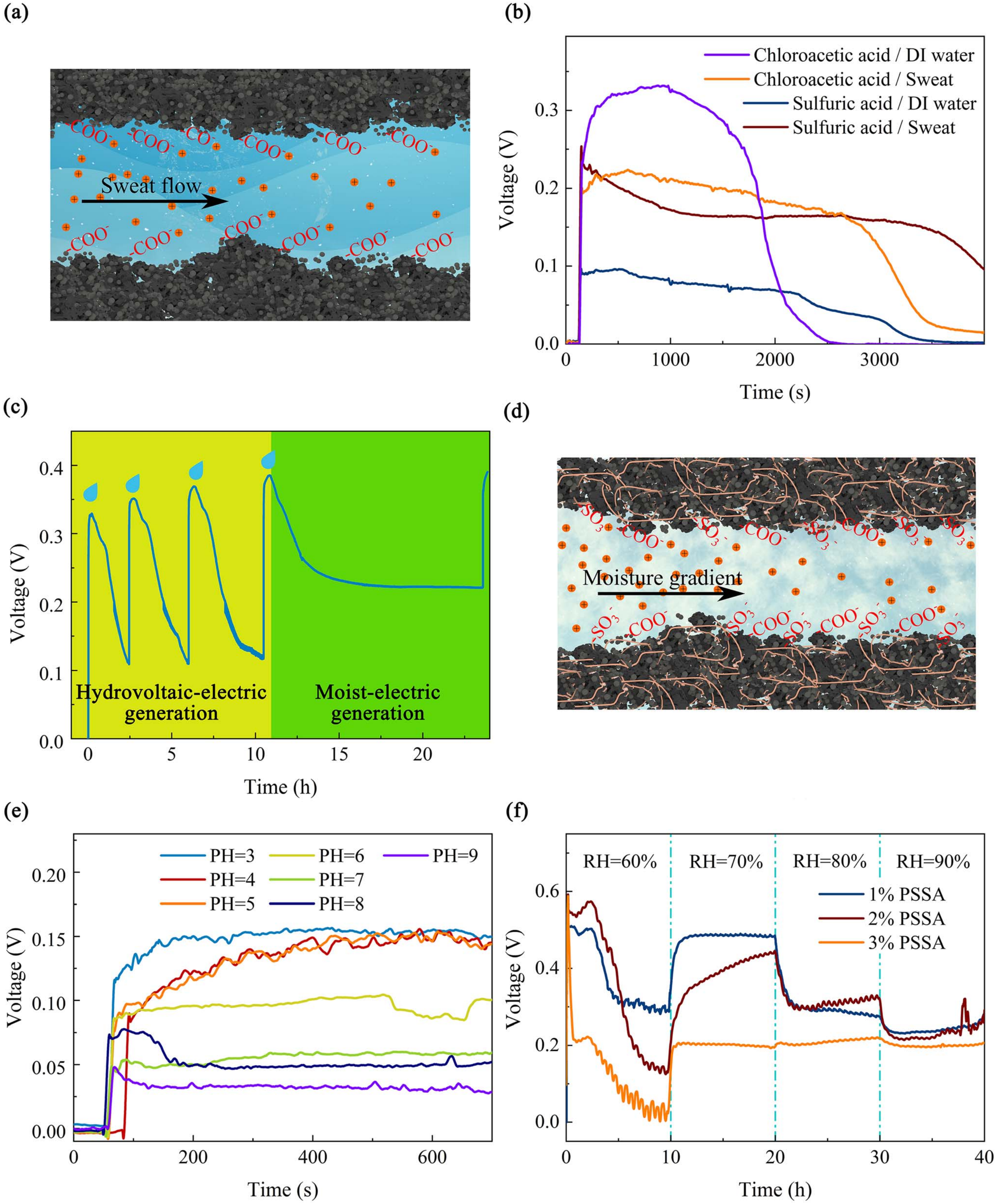

Fig. 3 The principle of hydrovoltaic electricity generation and moisture electricity generation and the nanogeneration performance of PPC papers. (a) Diagram of the principle of hydrovoltaic electricity generation. (b) Hydrovoltaic effect of PPC papers with different treatments, for DI water and sweat. (c) Tandem processes of hydrovoltaic electricity generation and moisture electricity generation on the same piece of PPC paper. (d) Diagram of the principle of moisture electricity generation. (e) Hydrovoltaic electricity generation for different pH values. (f) Moisture electricity generation in different moist environments by PPC papers treated with different concentrations of PSSA.

60%). The open-circuit voltages show a tendency of decreasing as the pH of the simulated sweat increases. The EDL allows only positively charged particles to pass through, and when the H^+ content increases, the amount of H^+ that can pass through the pores at the same water flow rate increases, resulting in a potential difference between upstream and downstream. Furthermore, the experiment confirmed the sensitivity of the PPC paper, which could serve as a sweat-pH sensor. In addition, the output voltage did not vary significantly with NaCl concentration in the hydrovoltaic electricity generation test (Fig. S9(b)†). This indicates that the PPC-paper device is not sensitive to the concentration of NaCl in simulated sweat, but only to pH, which helps its application in sweat-pH monitoring.

Subsequently, to verify previous speculations on the mechanism of moisture electricity generation, the test device that was previously dripped with 50 μL of simulated seawater was completely dried, and then in- and out-breaths applied over it, and with each breath, a rapid response in both open-circuit voltage and short-circuit current was observed (Fig. S10(a) and (b)†). In conclusion, the above experiments prove that the presence of hygroscopic ions will trigger moisture electricity generation in PPC papers. In order to investigate the factors affecting the moisture-electricity-generation performance of PPC papers, PPC papers were prepared and equal amounts of simulated sweat were dripped onto them to observe the output-voltage variation under different moist conditions over a long time (Fig. S11†). Firstly, PPC-paper-based moisture electricity generators with three different surface modification treatments (soaking in sulfuric-acid-mixture solution or chloroacetic-acid-mixture solution and oxygen-plasma bombardment) were prepared and all of them were placed in a constant temperature, moist test glove box. With 50 μL of simulated sweat solution added dropwise, and the moisture increased every 10 hours, their voltage outputs at 60%, 70%, 80% and 90% moisture are shown in Fig. S11(b).† In general, the generation voltage of the three surface-modified PPC papers decreased with increasing relative humidity (RH) in the air. The chloroacetic-acid-treated PPC paper device showed the least decrease, with voltage outputs of 0.22 V, 0.235 V, 0.2 V, and 0.19 V at 60%, 70%, 80%, and 90% RH, respectively. Chloroacetic acid-treated PPC grains carry more carboxyl groups, which facilitate the maintenance of high moisture electricity generation voltage at high moist.

To further investigate the effect of different polymers modified with PPC papers on the overall output voltage of the device, moisture electricity generation materials compounded with three polymers, namely polystyrene sulfonic acid (PSSA), polyvinyl alcohol (PVA) and sodium polyacrylate (PAAS), were prepared and their voltage outputs are shown in Fig. S12.† Among them, the PSSA composite device exhibits the best moisture-electricity-generation performance. After that, the moisture-electricity-generation performance of PPC papers treated with different concentrations of PSSA were tested separately, as shown in Fig. 3(f). Among them, the PPC paper treated with 1 wt% PSSA produces the highest electromotive force, about 500 mV, when the ambient humidity is 70%. However, the PPC paper treated with 3 wt% PSSA is not sensitive to humidity changes, and the generated electromotive force is relatively stable. For the moisture-electricity-generation device on 1% PSSA composite, the output voltage remains at 0 mV for the first 120 s due to the absence of water gradients and external stimuli. When simulated sweat is added dropwise at 120 s, the voltage rises rapidly to 500 mV. At this point, the driving force is provided primarily by the directional diffusion of simulated sweat. After 3 h, the capillary diffusion-driven hydrovoltaic effect diminishes as water evaporates from the device, resulting in a gradual reduction of the output voltage to 300 mV. By the end of 3 h, the ion-rich simulated sweat and the hygroscopic effect of ions tend to result in acquisition of moisture from the air, resulting in a moisture gradient at both ends of the device, and this gradient becomes the primary driver of moisture electricity generation during this phase. At the 10th hour of the test, the moisture increased to 70% RH and the water content in the environment increased rapidly, resulting in increased moisture absorption and a larger moisture gradient, which further increased the output voltage of the moisture electricity generator to 480 mV. After that, when the air moisture further increased to 80% and 90%, since the PPC paper can absorb moisture, the moisture gradient of the device decreased, and the output voltage decreased. Other polymer composites have similar mechanisms.[50,52,64]

2.3 The performance of each function of the SE-skin

In order to verify that the structural design was reasonable, we used COMSOL to simulate the state of sweat in the microfluidic channel, including flow rate, flow line and pressure, as shown in Fig. 4(a)–(c). The simulation results show that it is difficult for sweat in the microfluidic channel to enter each chamber because of the imbalance between the chamber and the external air pressure. Based on this, the structure of the microchannel has been improved, with a small hole added at the end of each chamber to balance the air pressure. The simulation results of the improved structure are shown in Fig. 4(d)–(f). It can be seen that sweat can enter each chamber in turn to meet the design requirements. As the untreated cured PDMS is hydrophobic, sweat does not flow out of the microfluidic channels through the small holes. To verify the simulation results, a physical experiment of sweat flow in the channel was performed, as shown in Fig. 4(g). In the microfluidic channel, the sweat flowed in exactly the same way and in exactly the same order as in the simulation results.

We designed the use of electrical signals generated by hydrovoltaic electricity generation to monitor the amount of sweat. Five pieces of PPC paper with hydrovoltaic electricity generation sections were placed in the corresponding chambers in the microfluidic channel and electrodes were used to connect the PPC papers to an external signal acquisition device to record the electrical signals generated on the PPC papers when sweat flowed through. The volume of the microfluidic channel is known and the rate of sweat collection in the microfluidic channel can be calculated from eqn (1)

$$v = \frac{\Delta V}{\Delta t} \tag{1}$$

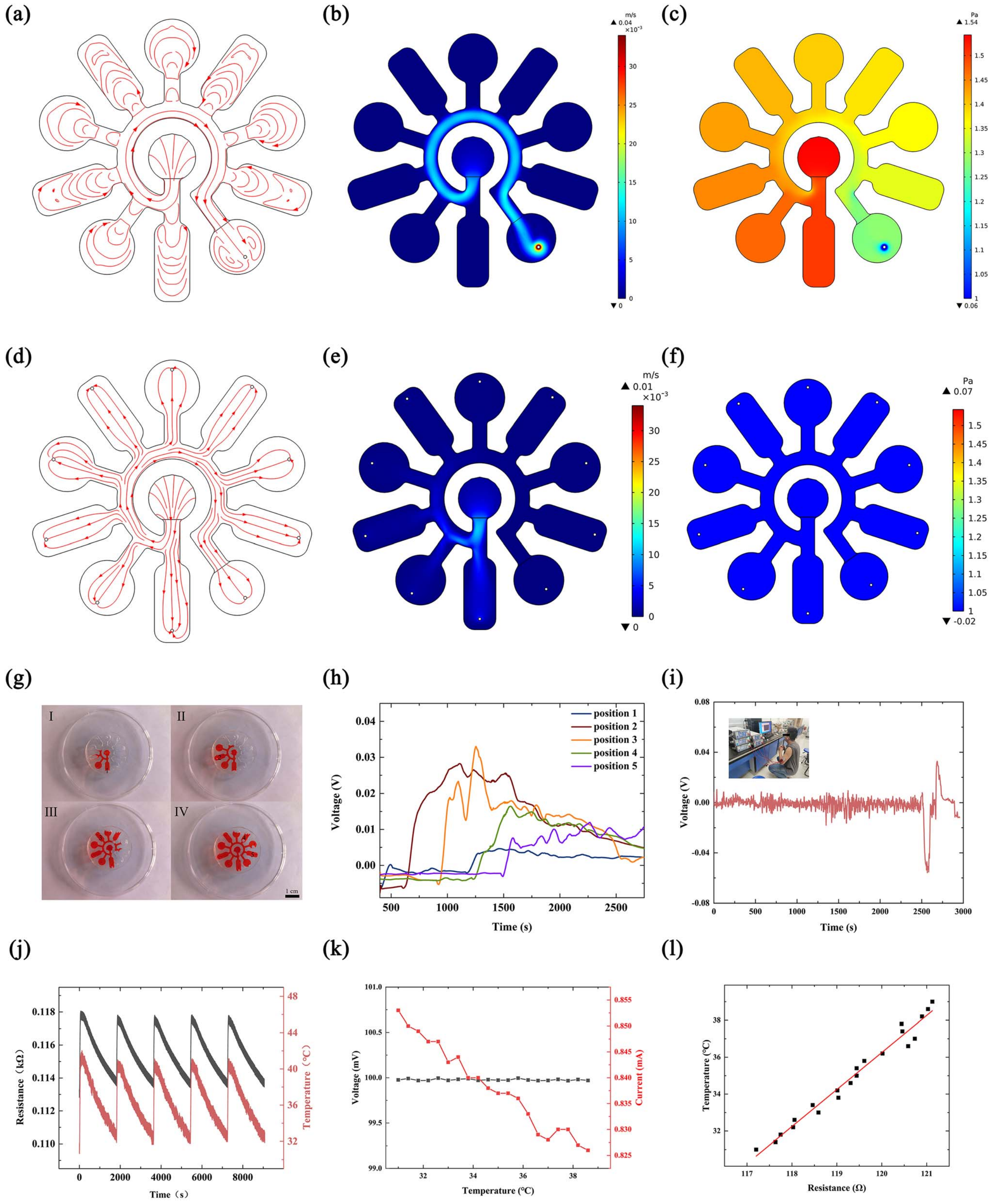

Fig. 4 Sweat flow monitoring and temperature measurement. Microfluidic channel simulation: (a) flow line, (b) flow rate and (c) pressure; improved device's (d) flow line, (e) flow rate and (f) pressure, which can reflect the progress of sweat flow in the microfluidic channel. (g) Physical flow of fluid through the microfluidic channel (the black numbers are the positions corresponding to the signals indicating the amount of sweat). (h) Real-time monitoring signals of sweat volume. (i) Experimental results of the SE-skin on the body. (j) Temperature-sensitive-resistor performance test; moisture electricity generation supply to the thermistor to measure temperature. (k) The change in voltage of the moisture electricity generator and current of the thermistor with temperature; (l) the change in the calculated resistance of the thermistor with temperature.

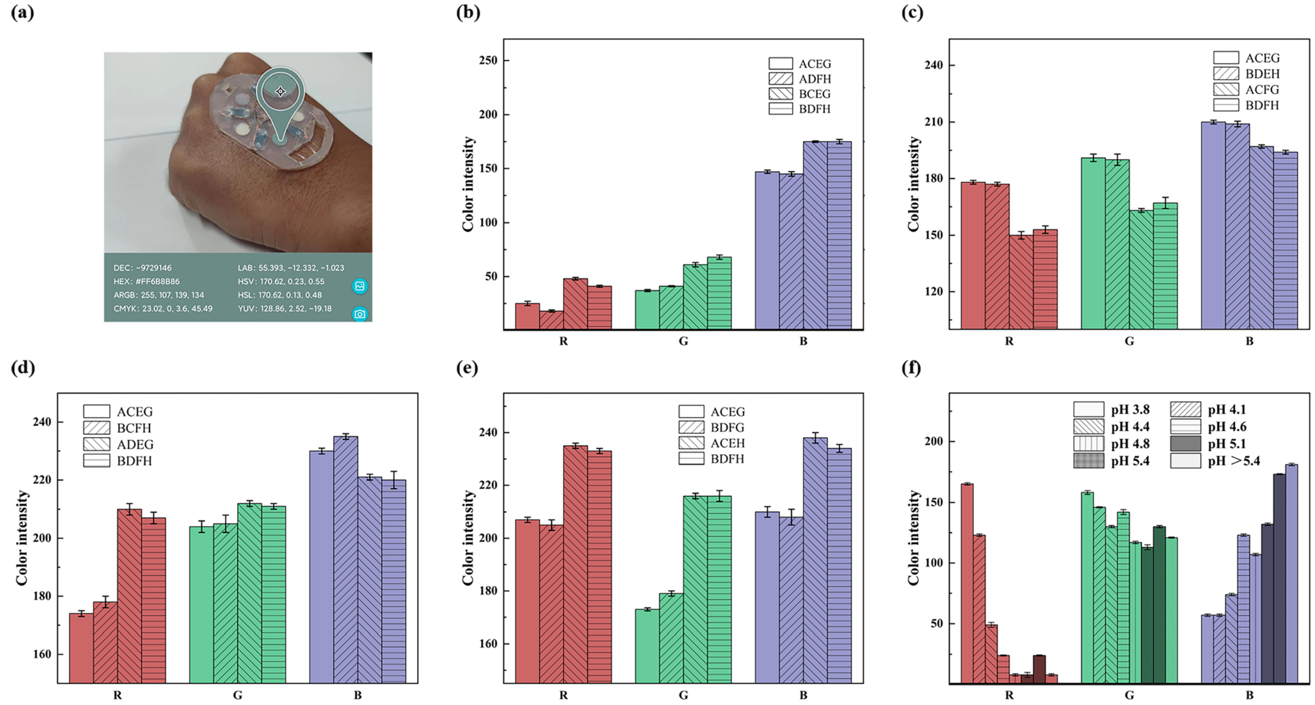

Fig. 5 Detection of physiological indicators in sweat. (a) Color recognition software detects color results in real time. The colored reaction of the colorimetric assay papers to different concentrations of (b) chloride ions, (c) uric acid, (d) glucose, (e) lactic acid and (f) pH is monitored.

where v represents the rate of sweat collection in the microfluidic channel, ΔV represents the volume of the microfluidic channel and Δt represents the time difference between the two electrical signals collected. The experiments monitoring the amount of sweat were carried out using simulated sweat, dripping at a uniform rate, and the results are shown in Fig. 4(h). The electrical signals were collected at around 300 s, 600 s, 900 s, 1200 s and 1500 s, demonstrating that the rate of sweat collection by the microfluidic channel is approximately the same over a long period of time when sweating at a uniform rate. This suggests that the amount of sweat collected in the microfluidic channel can be monitored using eqn (1) and the collected electrical signals, which helps us to monitor and analyze the sweating of the body over a certain period of time. By comparing sweating over multiple periods of time, the health status of the body can be analyzed. The SE-skin was fabricated with a thickness of 1 mm. Thus, the volume between two adjacent hydrovoltaic electricity generation chambers is estimated to be 109 μl. When a sudden change is detected in the hydrovoltaic electricity generation signal, it means that 109 μl of sweat has flowed into the corresponding chamber. Then we put the SE-skin on the body for testing, and the test results are shown in Fig. 4(i). Under the condition of continuous movement, the voltage is always about 0 V at the beginning, and the voltage shows a sudden change at about 2500 s, which proves that sweat flows into the first hydrovoltaic electricity generator chamber.

We have designed a function that uses moisture electricity generation to supply a thermistor for temperature testing of human skin. Moisture electricity generation can be used as a stable power source as it can generate electricity continuously for a considerable period of time and at a stable voltage. The temperature of the human skin in the corresponding area can be sensed in real time by collecting the electrical signals by mounting the temperature-sensitive resistor in the SE-skin so that it is in contact with the skin surface. We tested the thermistor performance in the interval around 30–45 °C, as shown in Fig. 4(j). The model of the thermistor is Pt100, and its main component is Pt. The resistance value of the thermistor corresponds well to its temperature. When the temperature rises, the resistance increases immediately, and when the resistance decreases, the resistance responds very quickly. Combined with the voltage generated by moisture electricity generation, the skin surface temperature can be measured without external power supply. After that, the thermistor that was supplied by the moisture electricity generation was tested to measure the temperature. Fig. 4(k) shows the changes in the voltage generated by the moisture electricity generator and in the current of the thermistor with temperature during operation. It can be seen from the figure that the voltage from the moisture electricity generation is relatively stable, and the current of the thermistor decreases gradually with temperature. Fig. 4(l) shows the resistance of the thermistor calculated at different temperatures. It can be seen from the figure that the resistance of the thermistor increases linearly with the increase of temperature. In addition, the moisture electricity generator integrated in the SE-skin was used to supply thermistors in order to detect the skin surface temperature. Fig. S13(a)† shows the surface temperature of human skin measured through the resistance of the thermistor powered by the moisture electricity generator integrated in the SE-skin. For comparison, the temperature in the glovebox was also measured by the SE-skin device, as illustrated in Fig. 4(l). Moreover, a real scenario was photographed for the measurement of human skin temperature, as shown in Fig. S13(b).†

Inside the SE-skin, the sweat flow process allows not only the amount of sweat to be monitored, but also the composition of many substances in the sweat to be detected. Colorimetric assay paper is an easy means to observe and analyze the detected substances and is well suited to the SE-skin. In addition, the color of the colorimetric assay paper can be detected and analyzed in real time using color recognition software on a mobile phone, resulting in an RGB value for the color of the colorimetric assay paper, which can be compared to the standard RGB value (Fig. 5) to analyze the amount of substances in the sweat. We fabricated various colorimetric assay papers for detecting substances in sweat and applied them in the flexible electronic device, as shown in Fig. 5(a).

Sweat contains a variety of substances that are all relevant to human health. We made five colorimetric assay papers to detect the content of chloride ions, uric acid, glucose and lactic acid, and the pH value of sweat. The performance of the colorimetric assay papers is shown in Fig. 5, where A represents chloride ions at a concentration of 0.01 g L^{-1}, B represents chloride ions at a concentration of 0.05 g L^{-1}, C represents glucose at a concentration of 1 mM, D represents glucose at a concentration of 0.1 mM, E represents uric acid at a concentration of 10 mg L^{-1}, F represents uric acid at a concentration of 50 mg L^{-1}, G represents lactic acid at a concentration of 10 mM, and H represents lactic acid at a concentration of 100 mM. Chloride ions are one of the most abundant substances in sweat; they reflect sweat health and are also associated with diseases such as cystic fibrosis. The normal level of chloride ions in human sweat is around 0.05 g L^{-1}, so we used a chemical reaction to create a colorimetric assay paper to detect the level of chloride ions. The results of its colored reaction in chloride ion solutions at concentrations of 0.01 and 0.05 g L^{-1} are shown in Fig. 5(b), which proves that it can be used to detect the amount of chloride ions in sweat. The color results can also be used to analyze the loss of electrolytes in the body during exercise. Uric acid is an important metabolite in the human body, and its excretion has a significant relationship with the health of the human body. The content of uric acid in normal human sweat is about 6 mg L^{-1}. Using the principle of redox reaction, we made a colorimetric assay paper for detecting the content of uric acid. Its colored reaction results for uric acid solutions of 10 and 50 mg L^{-1} are shown in Fig. 5(c). The results prove that it can be used to detect high levels of uric acid in sweat. Glucose is also an important excretion in sweat and its level in sweat is correlated with blood glucose, which can indirectly reflect whether the body has a disease that manifests as high blood glucose, like diabetes. The content of glucose in normal human sweat is in the range of 0.05–0.2 mM, so we use the redox reaction of glucose oxidase and catalase with glucose to make a colorimetric assay paper for detecting the glucose content between 0.1 and 1 mM. The colored reaction results in glucose solution are shown in Fig. 5(d). The results prove that it can detect the glucose content in sweat. In addition to the above substances in sweat, lactic acid is also an important sweat excretion, and its content in sweat can also reflect human health. The normal content of lactic acid in sweat is in the range of 5–20 mM, so we used lactate dehydrogenase to make a colorimetric assay paper to detect the lactic-acid content in sweat, and tested its color development in 10 and 100 mM lactic-acid solution. The reaction results are shown in Fig. 5(e), which proves that the prepared lactic-acid colorimetric assay paper can detect lactic acid within a certain concentration range. The pH value is also an important indicator in human sweat and its level directly reflects the health of the body. The pH value of normal human sweat is in the range of 4.5–5.5, so we used a pH assay paper with a detection range of pH 3.8–5.4 for detecting the pH value of sweat. The results of its colored reaction are shown in Fig. 5(f), which proved it to be sensitive in recognizing the pH value of sweat around the normal range. What is more, it can be seen from the figure that when the corresponding substance concentration of the colorimetric assay paper is the same, its RGB value has no relationship with that of other substances.

The basic principle of detecting the sweat components is that the substances in sweat undergo a chemical reaction with the substance in the colorimetric assay paper, resulting in a color change. The principle of the glucose colorimetric assay paper is that glucose in sweat forms gluconic acid and hydrogen peroxide under the catalysis of glucose oxidase, while hydrogen peroxide forms water and atomic oxygen under the catalysis of catalase. Atomic oxygen can oxidize chitosan to produce a colored reaction. The principle of the lactic-acid colorimetric assay paper is that lactic acid generates pyruvate and hydrogen peroxide under the action of lactate oxidase, while hydrogen peroxide releases atomic oxygen under the action of peroxidase. Atomic oxygen can oxidize chitosan to produce a colored reaction. The principle of the chloride-ion colorimetric assay paper is that ferrous ions generate iron ions under the action of chloride ions. The generated iron ions react with 2,4,6-tris(2-pyridyl)-*s*-triazine to form a coordination complex, resulting in a colored reaction. The principle of the uric-acid colorimetric assay paper is that uric acid is oxidized to allantoin and carbon dioxide by tungstic acid in alkaline solution, and phosphotungstic acid is reduced to tungsten blue in this reaction. The amount of tungsten blue generated is directly proportional to the uric-acid content in the reaction solution and can be determined by colorimetry.

We assembled the above modules to obtain a complete device for the SE-skin, as shown in Fig. S14.† The SE-skin will not deform after stretching (Fig. S15(a)†) or twisting (Fig. S15(b)†), and has a certain resistance to deformation, which can ensure long-term wear.

3. Experimental section

3.1 Materials

The PDMS and curing agent were purchased from Dow Corning, USA. 2,4,6-Tris(2-pyridyl)-*s*-triazine, Tween ® 80, mercury sulfate ($HgSO_4$), iron sulfate heptahydrate ($FeSO_4 \cdot 6H_2O$), 3,3′,5,5′-tetramethylbenzidine (TMB), phosphate buffer (pH 7.2–7.4), glucose oxidase from aspergillus niger and peroxidase from horseradish were from Aladdin. PSSA, PAAS, PVA, chitosan, acetic acid, methanol, and anhydrous ethanol were purchased from Maclean's. pH test strips were purchased from Shanghai San'aisi. The lactic acid kit and uric acid kit were purchased from Nanjing Jiancheng.

3.2 Preparation of microfluidic channel

Auto CAD was used to design the structure, then a laser was used to carve out the structure on 1 mm thick acrylic board to get an acrylic template. The acrylic template was cleaned, dried and treated with an oxygen-plasma cleaner for 2 min. The PDMS was mixed with the curing agent in a ratio of 10 : 1 and degassed in a vacuum drying oven. The acrylic template was placed in the mold, the degassed PDMS was poured in and the mold placed in a vacuum drying oven to degas. The degassed mold was placed on a heating plate and heated at 70 °C for 3 h to cure the PDMS. The cured PDMS was demolded, punched and cleaned with an oxygen-plasma cleaner for 2 min (Fig. 2(b)).

3.3 Preparation of PPC papers

The pomelo peel carbon powder dispersed in absolute ethanol was evenly spread on filter paper and put in a drying oven to dry. The carbon paper was soaked in the ink for 3 min and then dried in a drying oven. The carbon paper was then soaked in PSSA, PAAS or PVA for 5 min, and dried in a drying oven.

3.4 Preparation of colorimetric assay papers

Chloride colorimetric assay paper: a methanolic solution of 2,4,6-tris(2-pyridyl)-*s*-triazine (containing 0.8% Tween ® 80, w/w) at a concentration of 0.05 M and aqueous solutions of $HgSO_4$ and $FeSO_4$ at a concentration of 0.01 M were mixed in a ratio of 1 : 2 : 2, then the mixed solution was added dropwise to filter paper and dried. Glucose colorimetric assay paper: a 1 mg mL^{-1} solution of chitosan (containing 0.25% acetic acid, v/v) was added dropwise to filter paper and dried, then 3,3′,5,5′- tetramethylbenzidine (TMB) ethanol solution at a concentration of 15 mM was added dropwise to the filter paper and finally glucose oxidase and peroxidase solutions in phosphate buffer solution (concentrations of 180 μ mL^{-1} and 0.15 mg mL^{-1}) were added dropwise to the filter paper and dried. Lactate and uric acid colorimetric assay paper: the solutions in the lactate and uric acid kits were configured and dried by adding drops to filter paper in sequence. pH colorimetric assay paper: precise pH test strips were used, with a detection range of pH 3.8–5.4.

3.5 Preparation of electrode

The electrode structure was designed using Auto CAD and printed out on a microelectronic printer. The PPC papers and electrodes were connected using conductive silver paste and connected to the wires.

3.6 Tests on humans

The SE-skin was attached to the experimenter's arm and connected to the source meter. As the experimenter moved, the relevant data was detected. The experimenters were members of our research group and signed informed consent was obtained from them.

3.7 The composition of simulated sweat and seawater

The simulated sweat comprises histidine hydrochloride (17.5 g L^{-1}), sodium chloride (20 g L^{-1}), disodium hydrogen phosphate dodecahydrate (5 g L^{-1}) and lactic acid (15 g L^{-1}). The simulated seawater contains sodium chloride (24 g L^{-1}), magnesium chloride (11 g L^{-1}), sodium sulphate (4 g L^{-1}), calcium chloride (1 g L^{-1}), potassium chloride (0.7 g L^{-1}) sodium bicarbonate (0.2 g L^{-1}), potassium bromide (0.1 g L^{-1}), boric acid (0.027 g L^{-1}), strontium chloride (0.025 g L^{-1}) and sodium fluoride (0.003 g L^{-1}).

4. Conclusions

In summary, we first prepared PPC paper from domestic-waste pomelo peel and improved its performance, so that it had stable hydrovoltaic and moisture electricity generation performance, its performance reached the current average level of such materials, so it can be used as a stable power supply for electronic devices and real-time monitoring of sweat flow. According to the first proposed concept of integrating dual electricity generation into an electronic skin and using hydrovoltaic signals to monitor sweating, a multifunctional device with functions such as real-time monitoring of sweating, sweat-composition analysis and skin-surface temperature measurement was fabricated. Sweat is automatically collected during use, monitoring of the amount of sweat and sweat composition analysis can be performed autonomously, and the measurement of skin-surface temperature can be manually controlled and can last for a considerable period of time. The combination of two electricity generation modes (hydrovoltaic and moisture electricity generation) maximizes the use of sweat, which enables it to be self-driven and saves energy. Our SE-skin realizes the integration of the device and provides ideas for the design and manufacture of flexible electronic devices in the future. In the future, the combination of an SE-skin and NFC system will be realized to more conveniently monitor the health of human sweat in real time.

Conflicts of interest

There are no conflicts to declare.

Acknowledgements

This work was financially supported by the National Natural Science Foundation of China (No. 51871196 and 52071282), and the Yunnan Fundamental Research Projects (No. 202001BB050046). The authors thank the Advanced Analysis and Measurement Center of Yunnan University for the sample testing service and the Advanced Computing Center of Yunnan

University. The authors are grateful for the software support from Prof. Yingtang Zhou from Zhejiang Ocean University. Kai Han and Dadong Zhang contributed equally to this work.

References

1 Y. Song, D. Mukasa, H. Zhang and W. Gao, *Acc. Mater. Res.*, 2021, **2**, 184–197.

2 T. R. Ray, J. Choi, A. J. Bandodkar, S. Krishnan, P. Gutruf, L. Tian, R. Ghaffari and J. A. Rogers, *Chem. Rev.*, 2019, **119**, 5461–5533.

3 W. Gao, H. Ota, D. Kiriya, K. Takei and A. Javey, *Acc. Chem. Res.*, 2019, **52**, 523–533.

4 C. Xu, Y. Yang and W. Gao, *Matter*, 2020, **2**, 1414–1445.

5 Y. Liu, M. Pharr and G. A. Salvatore, *ACS Nano*, 2017, **11**, 9614–9635.

6 Q. Zheng, Q. Tang, Z. L. Wang and Z. Li, *Nat. Rev. Cardiol.*, 2021, **18**, 7–21.

7 W. Ji, J. Zhu, W. Wu, N. Wang, J. Wang, J. Wu, Q. Wu, X. Wang, C. Yu, G. Wei, L. Li and F. Huo, *Research*, 2021, **2021**, 9757126.

8 L. Xu, Z. Zhang, F. Gao, X. Zhao, X. Xun, Z. Kang, Q. Liao and Y. Zhang, *Nano Energy*, 2021, **81**, 105614.

9 J. Kim, E. F. Chou, J. Le, S. Wong, M. Chu and M. Khine, *Adv. Healthcare Mater.*, 2019, **8**, 1900109.

10 W. Gao, S. Emaminejad, H. Y. Y. Nyein, S. Challa, K. Chen, A. Peck, H. M. Fahad, H. Ota, H. Shiraki, D. Kiriya, D.-H. Lien, G. A. Brooks, R. W. Davis and A. Javey, *Nature*, 2016, **529**, 509–514.

11 A. Koh, D. Kang, Y. Xue, S. Lee, R. M. Pielak, J. Kim, T. Hwang, S. Min, A. Banks, P. Bastien, M. C. Manco, L. Wang, K. R. Ammann, K.-I. Jang, P. Won, S. Han, R. Ghaffari, U. Paik, M. J. Slepian, G. Balooch, Y. Huang and J. A. Rogers, *Sci. Transl. Med.*, 2016, **8**, 366ra165.

12 M. Elsherif, M. U. Hassan, A. K. Yetisen and H. Butt, *ACS Nano*, 2018, **12**, 5452–5462.

13 Y. Chen, S. Lu, S. Zhang, Y. Li, Z. Qu, Y. Chen, B. Lu, X. Wang and X. Feng, *Sci. Adv.*, 2017, **3**, e1701629.

14 Y. Yu, H. Y. Y. Nyein, W. Gao and A. Javey, *Adv. Mater.*, 2020, **32**, 1902083.

15 J. Kim, A. S. Campbell, B. E. de Ávila and J. Wang, *Nat. Biotechnol.*, 2019, **37**, 389–406.

16 Y. Lee, J. Park, A. Choe, S. Cho, J. Kim and H. Ko, *Adv. Funct. Mater.*, 2020, **30**, 1904523.

17 Z. Ma, S. Li, H. Wang, W. Cheng, Y. Li, L. Pan and Y. Shi, *J. Mater. Chem. B*, 2019, **7**, 173–197.

18 A. Ran, M. Cheng, S. Chen, Z. Liang, Z. Zhou, G. Zhou, F. Kang, X. Zhang, B. Li and G. Wei, *Energy Environ. Mater.*, 2022, DOI: 10.1002/eem2.12386.

19 H. Hou, K. M. Zeinu, S. Gao, B. Liu, J. Yang and J. Hu, *Energy Environ. Mater.*, 2018, **1**, 113–131.

20 T. R. Ray, J. Choi, A. J. Bandodkar, S. Krishnan, P. Gutruf, L. Tian, R. Ghaffari and J. A. Rogers, *Chem. Rev.*, 2019, **119**, 5461–5533.

21 J. Heikenfeld, A. Jajack, J. Rogers, P. Gutruf, L. Tian, T. Pan, R. Li, M. Khine, J. Kim, J. Wang and J. Kim, *Lab Chip*, 2018, **18**, 217–248.

22 H. C. Koydemir and A. Ozcan, *Annu. Rev. Anal. Chem.*, 2018, **11**, 127–146.

23 J. Kim, A. S. Campbell, B. E.-F. de Ávila and J. Wang, *Nat. Biotechnol.*, 2019, **37**, 389–406.

24 J. Li, J. Zhao and J. A. Rogers, *Acc. Chem. Res.*, 2019, **52**, 53–62.

25 G. Chen, Y. Li, M. Bick and J. Chen, *Chem. Rev.*, 2020, **120**, 3668–3720.

26 R. S. Ganesh, H. J. Yoon and S. W. Kim, *EcoMat*, 2020, **2**, e12065.

27 H. Chen, Y. Song, X. Cheng and H. Zhang, *Nano Energy*, 2019, **56**, 252–268.

28 W. Zhang, H. Guan, T. Zhong, T. Zhao, L. Xing and X. Xue, *Nano-Micro Lett.*, 2020, **12**, 105.

29 A. J. Bandodkar, P. Gutruf, J. Choi, K. Lee, Y. Sekine, J. T. Reeder, W. J. Jeang, A. J. Aranyosi, S. P. Lee, J. B. Model, R. Ghaffari, C.-J. Su, J. P. Leshock, T. Ray, A. Verrillo, K. Thomas, V. Krishnamurthi, S. Han, J. Kim, S. Krishnan, T. Hang and J. A. Rogers, *Sci. Adv.*, 2019, **5**, eaav3294.

30 S. B. Kim, K. Lee, M. S. Raj, B. Lee, J. T. Reeder, J. Koo, A. Hourlier-Fargette, A. J. Bandodkar, S. M. Won, Y. Sekine, J. Choi, Y. Zhang, J. Yoon, B. H. Kim, Y. Yun, S. Lee, J. Shin, J. Kim, R. Ghaffari and J. A. Rogers, *Small*, 2018, **14**, 1802876.

31 H. Li, T. Chang, Y. Gai, K. Liang, Y. Jiao, D. Li, X. Jiang, Y. Wang, X. Huang, H. Wu, Y. Liu, J. Li, Y. Bai, K. Geng, N. Zhang, H. Meng, D. Huang, Z. Li, X. Yu and L. Chang, *Nano Energy*, 2022, **92**, 106786.

32 Y. Bi, M. Sun, J. Wang, Z. Zhu, J. Bai, M. Y. Emran, A. Kotb, X. Bo and M. Zhou, *Anal. Chem.*, 2023, **95**, 6690–6699.

33 X. Pei, M. Sun, J. Wang, J. Bai, X. Bo and M. Zhou, *Small*, 2022, **18**, 2205061.

34 J. T. Reeder, J. Choi, Y. Xue, P. Gutruf, J. Hanson, M. Liu, T. Ray, A. J. Bandodkar, R. Avila, W. Xia, S. Krishnan, S. Xu, K. Barnes, M. Pahnke, R. Ghaffari, Y. Huang and J. A. Rogers, *Sci. Adv.*, 2019, **5**, eaau6356.

35 S. Kim, B. Lee, J. T. Reeder, S. H. Seo, S. U. Lee, A. Hourlier-Fargette, J. Shin, Y. Sekine, H. Jeong, Y. S. Oh, A. J. Aranyosi, S. P. Lee, J. B. Model, G. Lee, M. H. Seo, S. S. Kwak, S. Jo, G. Park, S. Han, I. Park, H. I. Jung, R. Ghaffari, J. Koo, P. V. Braun and J. A. Rogers, *Proc. Natl. Acad. Sci. U. S. A.*, 2020, **117**, 27906–27915.

36 S. B. Kim, Y. Zhang, S. M. Won, A. J. Bandodkar, Y. Sekine, Y. Xue, J. Koo, S. W. Harshman, J. A. Martin, J. M. Park, T. R. Ray, K. E. Crawford, K. T. Lee, J. Choi, R. L. Pitsch, C. C. Grigsby, A. J. Strang, Y. Y. Chen, S. Xu, J. Kim, A. Koh, J. S. Ha, Y. Huang, S. W. Kim and J. A. Rogers, *Small*, 2018, **14**, 1703334.

37 J. Choi, A. J. Bandodkar, J. T. Reeder, T. R. Ray, A. Turnquist, S. B. Kim, N. Nyberg, A. Hourlier-Fargette, J. B. Model, A. J. Aranyosi, S. Xu, R. Ghaffari and J. A. Rogers, *ACS Sens.*, 2019, **4**, 379–388.

38 A. J. Bandodkar, W. J. Jeang, R. Ghaffari and J. A. Rogers, *Annu. Rev. Anal. Chem.*, 2019, **12**, 1–22.

39 R. Ghaffari, J. Choi, M. S. Raj, S. Chen, S. P. Lee, J. T. Reeder, A. J. Aranyosi, A. Leech, W. Li, S. Schon, J. B. Model and J. A. Rogers, *Adv. Funct. Mater.*, 2020, **30**, 1907269.
40 V. Hessel, M. M. Sarafraz and N. N. Tran, *Chem. Eng. Sci.*, 2020, **225**, 115774.
41 A. G. Niculescu, C. Chircov, A. C. Birca and A. M. Grumezescu, *Int. J. Mol. Sci.*, 2021, **22**, 2011.
42 H. Ma, F. Lv, L. Shen, K. Yang, Y. Jiang, J. Ma, X. Geng, T. Sun, Y. Pan, Z. Xie, M. Xue and N. Zhu, *Energy Environ. Mater.*, 2022, **5**, 986.
43 Q. Yang, Y. Wang, X. Li, H. Li, Z. Wang, Z. Tang, L. Ma, F. Mo and C. Zhi, *Energy Environ. Mater.*, 2018, **1**, 183–195.
44 Q. Cao, B. Liang, X. Mao, J. Wei, T. Tu, L. Fang and X. Ye, *Electroanalysis*, 2020, **33**, 643–651.
45 Y. Su, L. Lu and M. Zhou, *ACS Appl. Mater. Interfaces*, 2022, **14**, 8664–8668.
46 J. Wang, M. Sun, X. Pei, L. Zheng, C. Ma, J. Liu, M. Cao, J. Bai and M. Zhou, *Adv. Funct. Mater.*, 2022, **32**, 2209697.
47 Z. Ning, Z. Long, G. Yang, L. Xing and X. Xue, *Biosensors*, 2022, **12**, 164.
48 G. Xue, Y. Xu, T. Ding, J. Li, J. Yin, W. Fei, Y. Cao, J. Yu, L. Yuan, L. Gong, J. Chen, S. Deng, J. Zhou and W. Guo, *Nat. Nanotechnol.*, 2017, **12**, 317–321.
49 L. Li, M. Hao, X. Yang, F. Sun, Y. Bai, H. Ding, S. Wang and T. Zhang, *Nano Energy*, 2020, **72**, 104663.
50 W. Wang, W. Gong, Y. Wang, G. Li, W. Lu, Y. You and X. Zhang, *J. Mater. Chem. A*, 2021, **9**, 5588–5596.
51 Z. Feng, W. Zhao, Z. Yang, Y. Deng, T. Yang and Y. Ni, *J. Mater. Chem. A*, 2022, **10**, 11524–11534.
52 Z. Sun, L. Feng, C. Xiong, X. He, L. Wang, X. Qin and J. Yu, *J. Mater. Chem. A*, 2021, **9**, 7085–7093.
53 Q. Lyu, B. Peng, Z. Xie, S. Du, L. Zhang and J. Zhu, *ACS Appl. Mater. Interfaces*, 2020, **12**, 57373–57381.
54 Y. Miyoshi, K. Miyajima, H. Saito, H. Kudo, T. Takeuchi, I. Karube and K. Mitsubayashi, *Sens. Actuators, B*, 2009, **142**, 28–32.
55 J. T. Reeder, Y. Xue, D. Franklin, Y. Deng, J. Choi, O. Prado, R. Kim, C. Liu, J. Hanson, J. Ciraldo, A. J. Bandodkar, S. Krishnan, A. Johnson, E. Patnaude, R. Avila, Y. Huang and J. A. Rogers, *Nat. Commun.*, 2019, **10**, 5513.
56 Z. Zhang, X. Li, J. Yin, Y. Xu, W. Fei, M. Xue, Q. Wang, J. Zhou and W. Guo, *Nat. Nanotechnol.*, 2018, **13**, 1109–1119.
57 F. Zhao, Y. Liang, H. Cheng, L. Jiang and L. Qu, *Energy Environ. Sci.*, 2016, **9**, 912–916.
58 T. Xu, X. Ding, C. Shao, L. Song, T. Lin, X. Gao, J. Xue, Z. Zhang and L. Qu, *Small*, 2018, **14**, 1704473.
59 C. Yang, Y. Huang, H. Cheng, L. Jiang and L. Qu, *Adv. Mater.*, 2019, **31**, 1805705.
60 J. Bai, Y. Huang, H. Cheng and L. Qu, *Nanoscale*, 2019, **11**, 23083–23091.
61 F. Zhao, H. Cheng, Z. Zhang, L. Jiang and L. Qu, *Adv. Mater.*, 2015, **27**, 4351–4357.
62 D. Shen, W. W. Duley, P. Peng, M. Xiao, J. Feng, L. Liu, G. Zou and Y. N. Zhou, *Adv. Mater.*, 2020, **32**, 2003722.
63 T. Xu, X. Ding, Y. Huang, C. Shao, L. Song, X. Gao, Z. Zhang and L. Qu, *Energy Environ. Sci.*, 2019, **12**, 972–978.
64 X. Liu, H. Gao, J. E. Ward, X. Liu, B. Yin, T. Fu, J. Chen, D. R. Lovley and J. Yao, *Nature*, 2020, **578**, 550–554.